GCM experiments on changes in atmospheric predictability associated with the PNA pattern and tropical SST anomalies

By JIAN SHENG, *Canadian Centre for Climate Modelling and Analysis, Meteorological Service of Canada, PO Box 1700, Victoria, B.C. V8W 2Y2, Canada*

ABSTRACT

Based on results from a simple three-level quasi-geostrophic model, Lin and Derome suggested that atmospheric predictability is influenced by the Pacific/North American (PNA) pattern. In the present study, predictability experiments are conducted with the Canadian Centre for Climate Modelling and Analysis general circulation model (CCCma GCM). A 47-yr integration of the GCM with specified sea surface temperature (SST) for the years 1948–94 is first performed. Forecasts are initiated whenever the PNA pattern is in a strong positive or strong negative phase during this simulation. For each forecast, an ensemble of six initial conditions is generated with small random perturbations. Forecasts initiated when the PNA is in its positive phase have smaller growth rates of ensemble standard deviation than forecasts initiated when the PNA is in its negative phase. Regional characteristics of the prediction spread are also examined. Similar experiments are conducted to determine the relationship between atmospheric predictability and SST anomalies in the tropical Pacific. Forecasts initiated when tropical SST anomalies are positive have smaller growth rates of ensemble standard deviation than forecasts initiated when tropical SST anomalies are negative. However, cases with positive tropical SST anomalies but without a strong PNA pattern show a similar prediction spread to cases with negative SST anomalies. The results suggest that, in comparison to the PNA pattern, the influence of tropical SST anomalies is only secondary. A set of three-layer diagnostic equations is used to analyze the GCM results. It is speculated that the transient eddies have a stronger influence on the circulation anomalies (and therefore reduce the atmospheric predictability more) in the negative PNA phase than in the positive PNA phase.

1. Introduction

In his celebrated papers, Lorenz (1963, 1969) discussed the uncertainties related to the atmospheric governing equations, which lead to the concept of an ultimate time limit in which skilled predictions of atmospheric evolution can be made by a deterministic dynamic forecast model. The existence of such a limit on atmospheric predictability results from the combination of the nonlinear

---

* Corresponding author.
e-mail: jian.sheng@ec.gc.ca

nature of the dynamic system and an inevitable presence of errors in the initial conditions, boundary conditions and model equations. Early, perhaps overly optimistic estimates of the limit are about two weeks for the predictions of synoptic-scale flow (Charney et al., 1966; Smagorinsky, 1969).

The uncertainties of atmospheric predictions can be addressed by making an ensemble of forecasts started from slightly different initial conditions. Epstein (1969) and Leith (1974) attempted to measure the sensitivity of stochastic–dynamic forecasts to initial condition errors and therefore, evaluate the confidence of the forecasts. Spatial

and time averages have been used to make filtered extended-range forecasts. When different average processes are taken, rapid growth of initial errors associated with the high-frequency eddies is reduced, although the synoptic scale flow is no longer predicted, as in a single forecast.

In a more recent effort (Derome et al. 2001), forecasts made by a numerical weather prediction model and by a general circulation model (GCM) are linearly combined to extend the experimental dynamic forecasts up to a season. The coefficients of the linear combination depend on the coefficients of leading empirical orthogonal functions (EOFs) of the forecasts from the two models.

For a specific model, considerable case-to-case variations exist in the predictability of the atmospheric evolution in the extended range. Presumably certain types of flow configurations are inherently more predictable and hence amenable to deterministic forecast methods than other types. Furthermore, model weaknesses may have a less negative influence on the predictability of some dynamic structures. Miyakoda et al. (1986) discussed a number of one-month predictions of the GFDL (Geophysical Fluid Dynamics Laboratory) model and reported significant variability on predictability from year to year. Branstator et al. (1993) attempted to identify low-frequency circulation components that are highly predictable in medium- and extended-range numerical forecasts. These studies generally support the notion that predictability can be enhanced if favorable flow patterns prevail.

Among other atmospheric configurations, the Pacific/North American (PNA) pattern has received particular attention. Palmer (1988) found that the prediction skill of the medium-range forecasts from the ECMWF (European Centre for Medium-Range Weather Forecasts) is correlated with the PNA index. The increased instability was explained with a barotropic model. More recently, Lin and Derome (1996) discussed changes in predictability associated with the PNA pattern in a three-level T21 quasi-geostrophic (Q-G) model. They performed a large number of forecast experiments showing that predictability is higher during the positive PNA phase than that during the negative phase. This was shown in the sense of a global average, but the signal was particularly strong over the North Pacific, North American and the North Atlantic regions.

In the present paper, the relationship between the predictability and the PNA pattern is investigated in a perfect model context using the Canadian Centre for Climate Modelling and Analysis (CCCma) general circulation model (GCM). Using a GCM to study atmospheric predictability has some advantages compared to a simple model or an operational forecast model. The GCM has sophisticated physical parameterization schemes in comparison to simple models, such as the quasi-geostrophic model of Lin and Derome (1996) and therefore provides a more comprehensive platform to test the relationship between the PNA pattern and predictability. The CCCma GCM is a uniform test ground for multi-year forecast experiments. As operational models are frequently modified and presumably improved, it is difficult to distinguish the effects of model changes from that of PNA pattern when we compare predictions for more than just a few years.

In addition to the PNA pattern, the relationship between the predictability and the sea surface temperature (SST) anomalies in the equatorial Pacific is also examined in the present study. Chen (1990) showed that the prediction skill of the National Meteorological Center medium-range forecasts was higher over the PNA sector during the El Niño winters than during non-El Niño winters. Since the PNA pattern has a good correlation with the tropical SST anomalies (Horel and Wallace, 1981), the relative importance of the two factors will be compared in our forecast experiments.

The paper is organized into sections as follows. The model and GCM experiments are described in Section 2. In Section 3, the relationship between the tropical SST anomalies and the PNA pattern simulated by the GCM is investigated with the singular value decomposition (SVD) analysis. Prediction spread of model experiments for different PNA phases is presented Section 4. The results are summarized in Section 5.

2. Model and experiment design

The prediction experiments in the present paper are made with the Canadian Centre for Climate Modelling and Analysis second-generation general circulation model (GCMII). The model has been documented by McFarlane et al. (1992) and used

for climate change simulations as discussed by Boer et al. (1992). CCCma GCMII has ten vertical levels (L10) and a triangularly truncated spectral representation of 32 longitudinal waves (T32). During the model integration, SST and sea-ice boundary are specified by observed mean monthly values from the GISST (Global sea-Ice and Sea Surface Temperature) data set, which is compiled and processed by the Hadley Centre of the UK Meteorological Office. CCCma GCMII uses an improved scheme for the time interpolation of SST such that the observed mean monthly values are preserved in the model output (Sheng and Zwiers, 1998). CCC GCMII has also been coupled to a dynamic ocean general circulation model and u! sed to perform a number of climate change simulations (Flato et al., 2000; Boer et al., 2000a; 2000b).

Prior to the prediction experiment, a 47-yr (1948–1994) integration of the model is carried out using the GISST sea surface temperature and sea-ice extent information as the boundary condition. The climatology and low-frequency variability of the simulation are discussed in Zwiers et al. (1999). This 47-yr GISST integration provides the background atmospheric conditions for the extended forecast experiments.

In the present study, a forecast experiment is initiated for a winter month (December, January or February) only if the model atmosphere for the previous month (November, December or January) is in a strong PNA phase or strong SST anomalies exist in the tropical Pacific. The use of PNA or SST information from the previous months imitates the operational mode of long-term forecasts, in which observed monthly means are not available for the forecast period. The persistence of PNA index implies that a strong PNA pattern in the previous month will most likely be followed by a similar pattern during the current month, and so does the persistence of SST anomalies. Detailed criteria for selecting the months for the forecast experiments are discussed in Section 4.

The experiments are designed such that the predictions are started only after a strong PNA pattern has already been established. This approach is somewhat different from the one adopted in Lin and Derome (1996), in which predictions are compared in the same period a strong PNA pattern is in existence. The practical

significance of our approach is that the results of this study provide a method to assess the confidence of extended-range forecasts before the prediction actually starts.

Once a month is selected for the prediction experiment, an ensemble of six (6) forecasts is made with the same specified bottom boundary condition but different initial conditions, perturbed by the introduction of small errors. To generate the six different initial conditions, all variables in the model 'restart file', which stores all the variables necessary to continue an ongoing integration, are randomly perturbed. The formula for the initial condition follows Schubert and Suarez (1989):

$$f^* = f + \varepsilon(f^{(2)} - f^{(1)}), \tag{1}$$

where, $\varepsilon = 0.01$, $f^{(1)}$ and $f^{(2)}$ are variables at the same calendar day but two different, randomly chosen years. Perturbations introduced by Eq. (1) generate six different initial states, which provide the prediction uncertainties needed for the ensemble forecasts. The random perturbation method turns out to be very successful, as all branched time integrations restart quite smoothly without noticeable imbalances. This process is schematically illustrated in Fig. 1.

Each forecast lasts 20 d, since no forecast skill remains afterward. We take the perfect model approach as in Lin and Derome (1996), and the predictability is assessed by the standard deviation
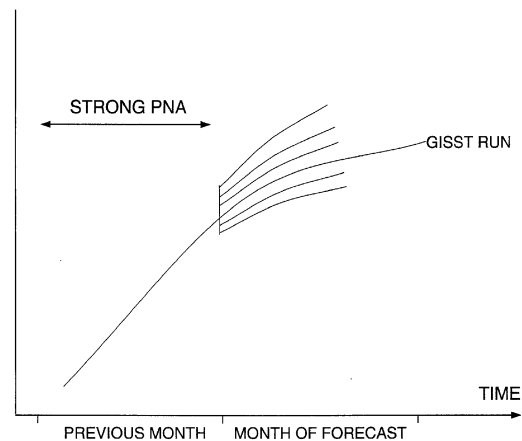

Fig. 1. Schematic illustration of the prediction experiments.

within each forecast ensemble:

$$S = \left[\frac{1}{(n-1)} \sum_j \left(\bar{z}_j - \frac{1}{n} \sum_k \bar{z}_k \right)^2 \right]^{1/2}, \qquad (2)$$

where n is the size of the ensemble prediction, z is the geopotential height at model vertical level $\eta = 0.542$, subscripts j and k index the forecasts within an ensemble, and $(\bar{\ })$ is a 5 d time average. Under the perfect model approach, the standard deviation S is a measure of prediction spread, and therefore a measure of forecast sensitivity to errors introduced in initial conditions. A lower value of S indicates a higher confidence in the ensemble forecasts, and therefore a higher predictability with a perfect model.

The ensemble size $n = 6$ is used in the present study. Although a larger ensemble size is preferred in calculating the prediction spread of individual ensemble, our results are reasonably stable because all calculations shown in Section 4 are based on averages of 20 ensembles and each ensemble contains six forecasts.

3. SVD analysis of GCM Results

The technique of singular value decomposition (SVD) is applied to the SST anomalies and the 500 hPa geopotential height fields simulated by the CCCma GCMII. By objectively isolating pairs of spatial patterns of SST and height fields that have the highest covariance, the SVD analysis identifies patterns that tend to occur synchronously with one another. Theoretical and practical aspects of SVD can be found in Bretherton et al. (1992).

The purpose of the SVD analysis is to verify that the GCM simulates the well known PNA pattern in the 47-yr GISST integration and reproduces the positive correlation between the SST anomalies in the equatorial Pacific and the midlatitude PNA pattern (Horel and Wallace, 1981). In addition, the SVD analysis generates time series of the PNA pattern and SST anomalies as the projections of the original data sets onto the SVD modes, which will be used later to select the months for the prediction experiments.

The domain of SST for the SVD analysis is limited to the tropical Pacific between 20°N and 20°S. Monthly mean SST fields are projected onto the model Gaussian grid. Simulated 500 hPa geo-

potential is interpolated from the model Gaussian grid to a 51×55 Northern Hemisphere polar stereographic grid. Mean monthly anomalies are obtained by removing the 47-yr climatology of the month from the model monthly mean time series. The SVD analysis covers the November, December and January period with $3 \times 47 = 141$ months in total.

Principal component analysis (PCA) is applied to SST and geopotential prior to the SVD analysis, and only the first ten eigenvectors from each dataset are retained as input for SVD. Retained eigenvectors explain 85 and 89% of the total variance for the SST and geopotential fields, respectively. A sensitivity study of SVD has been carried out with eight retained eigenvectors for both SST and geopotential, and the results are virtually unchanged (not shown).

The covariance matrix for SVD is calculated with the retained eigenvectors as the input time series. The first mode explains roughly 66% of the squared covariance, and the temporal correlation coefficient between the time series of SST and geopotential is about 0.38. We will ignore all other modes in this study.

Figure 2a shows the structure of the first SVD mode for the 500 hPa geopotential. It has the familiar structure of the observed PNA pattern, except that the subtropical center in the Pacific, which is outside of the analysis grid, is not very well defined. The first SVD mode of SST anomalies (Fig. 2b) is a warm temperature tongue in the tropical eastern Pacific, reminiscent of the SST structure during the El Niño episodes.

On summary, the SVD analysis shows that, with the bottom boundary conditions specified by the GISST data set, the CCCma GCMII demonstrates a reasonable simulation of the observed midlatitude PNA pattern in terms of its spatial structure. The model PNA pattern is positively correlated with the tropical Pacific SST anomalies, in agreement with the observations. Simulations of the PNA and other low-frequency patterns in CCCma GCMII have been reported in Zwiers et al. (1999).

Since the first mode of SVD represents the combined signal of El Niño and PNA pattern in the model, we will use the two time series of the SST and geopotential as indexes to select a month as the period of strong PNA phase or SST anomalies.
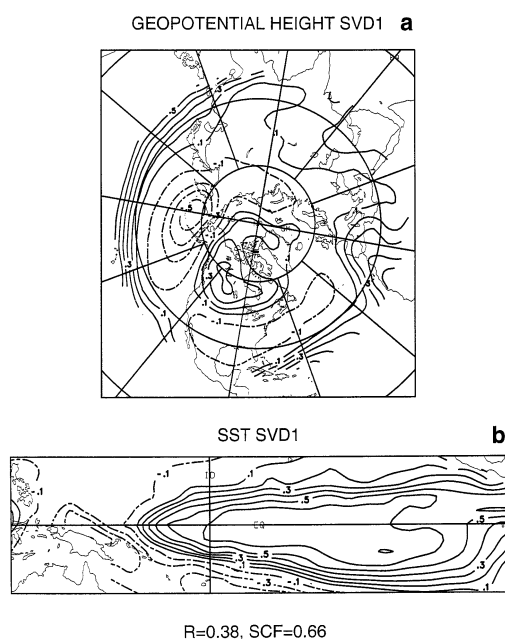
GEOPOTENTIAL HEIGHT SVD1 **a**

SST SVD1 **b**

R=0.38, SCF=0.66

Fig. 2. (a) Spatial height pattern of the first SVD modes as the correlation between the height expansion coefficients and the height anomalies. (b) As in (a) but for SST anomalies. Contour interval 0.1.

4. Results of prediction experiments

In Fig. 3 the solid curve shows the prediction spread S as a function of forecast length, averaged over the polar cap north of 20°N and over all prediction ensembles, including all the experiments in $+$PNA, $-$PNA, $+$SST and $-$SST (see definitions below) groups. The vertical bars represent the standard deviation of S among the ensembles. The horizontal dashed line of 74.6 m is the climatological standard deviation of the geopotential. The model forecasts show considerable variability of prediction spread in time. Since the prediction spread is measured in terms of the standard deviation within each forecast ensemble, the rising trend with time indicates the gradual increase of uncertainty due to the initial random perturbation and the loss of predictability. Figure 3 shows that during the first 5 d the standard deviation increases gradually. This increase accelerates between day 5 and day 15 and finally levels off after day 15. It can be seen that the prediction spread, on average, reaches the climatological value at about 12.8 d. After that, the predictions
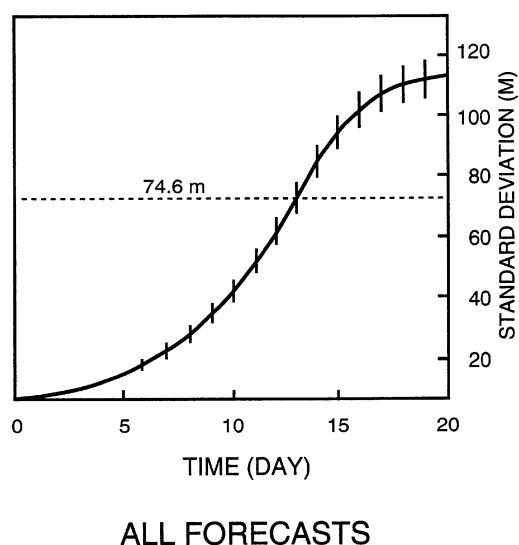

ALL FORECASTS

Fig. 3. Mean and standard deviation of the prediction scores as functions of time. Units in meters.

lose their practical values, on average, although the implied correlation of 0.5 is not negligible for some applications. As we will show next, however, the prediction spread varies considerably from case to case.

In the first experiment (EXP1), we stratify individual months in the winter season according to the strength of the PNA pattern. The time series of the first SVD mode for the SST and 500 hPa geopotential are shown in Fig. 4 as a scatter diagram. The abscissa measures the amplitude of tropical SST anomalies and the ordinate, the PNA pattern. From the 141 months represented by small crosses, a positive correlation can be observed between the PNA and SST time series from the model simulation.

The 20 months with the highest PNA projections are selected as Group $+$PNA. They are enclosed in the upper dashed box in Fig. 4. Similarly, the 20 months with the lowest PNA projections are enclosed in the lower dashed box as Group $-$PNA. The difference of the mean projection coefficients between the $+$PNA and $-$PNA groups is 2.3 for geopotential and 1.4 for SST (Fig. 4).

The months included in $+$PNA and $-$PNA are selected as the starting months of the forecast experiments. For each month in the two groups, six forecasts are started at the first day of the
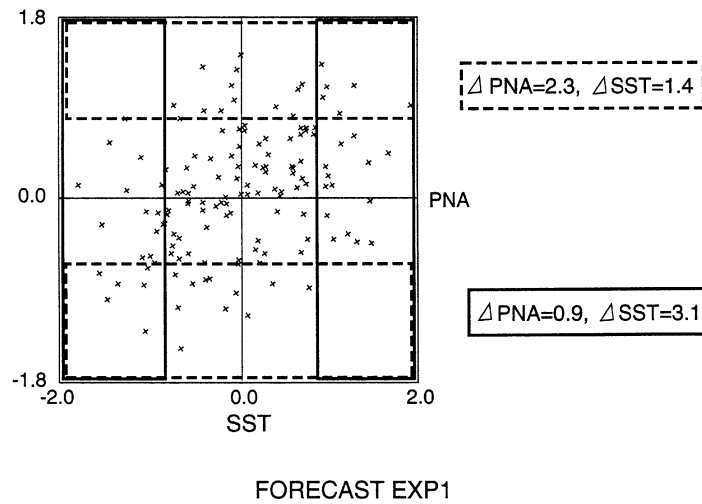
FORECAST EXP1

Fig. 4. EXP1. Scatter diagram of the time series of the first SVD mode for the SST and 500 hPa geopotential. The abscissa represents SST and the ordinate, geopotential. Non-dimensional units. The 20 months of the highest and the lowest PNA projections are enclosed in the upper and lower rectangular boxes, respectively. The 20 months of the highest and the lowest SST projections are enclosed in the right and left boxes.

following month, with the perturbed initial conditions described in Section 2. Each forecast continues for 20 days, beyond which no predictability exists based on the criteria of climatological standard deviation we adopted.

Figure 5 shows the spread as a function of prediction length, averaged over the polar cap north of 20°. The thick solid curve in Fig. 5 represents the mean spread for the 20 forecasts in the +PNA group, and the thin solid curve, that

in the −PNA group. We see that during the first a few days of the forecasts, the two curves are hard to separate. After day 5, however, the +PNA group shows consistent lower prediction spread during the rest of the 20-d forecast period. The improvement on the time limit of skillful forecast is about 1.4 d, measured by the time for the prediction spread to reach the value of the climatological standard deviation.
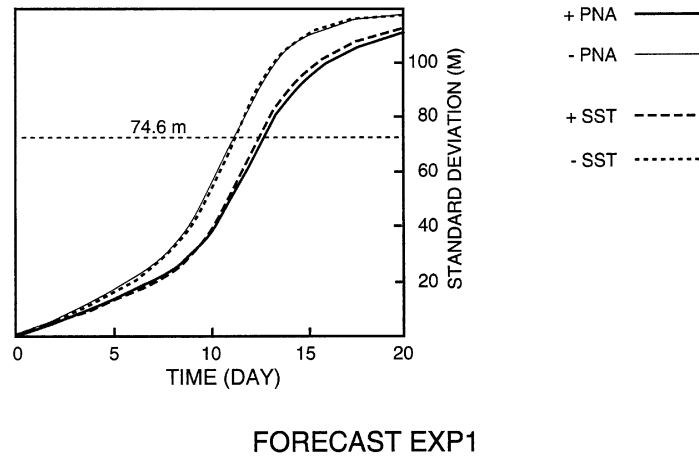
Similarly, we stratify individual months accord-

FORECAST EXP1

Fig. 5. EXP1. Prediction score as functions of time.

ing to the SST anomalies in the tropics. In the scatter diagram (Fig. 4), the 20 months with the highest (lowest) SST projections are enclosed in the right (left) solid box for the +SST (−SST) group. The difference in the mean projection coefficients between the +SST and −SST groups is 0.9 for geopotential and 3.1 for SST (Fig. 4).

Results for predictions made during winter months with strong SST anomalies are also shown in Fig. 5. The +SST group, represented by the dashed curve, outperforms the -STT group (the dotted curve) significantly after day 5 of the forecast period. The improvement on the predictability is roughly 1.3 d.

In light of the positive correlation between the PNA pattern and the tropical SST anomalies, the results for the +SST and −SST groups are not surprising, since many cases included in the +SST (−SST) group are also found in +PNA (−PNA) group.

A second forecast experiment (EXP2) is designed to examine the relationship between the predictability and initial conditions, excluding the correlation between the PNA pattern and tropical SST anomalies. In this experiment, the +PNA group is selected as the 20 months which show the highest PNA time coefficients but do not belong to the group with top 20 SST projections. This is shown in Fig. 6 as crosses enclosed in the upper dashed box. Similarly the −PNA group is

selected as the 20 months inclosed in the lower dashed box in Fig. 6.

The results of the +PNA and −PNA groups are shown in Fig. 7 as functions of time. The forecasts for the +PNA group again outperform that for the −PNA group during most of the 20-d forecast period, in good agreement with EXP1, indicating that the phase of the PNA pattern has a strong impact on the predictability, with or without the presence of strong SST anomalies in the tropical Pacific.

We also examined the relationship between the predictability and the tropical SST anomalies excluding the influence of the PNA and tropical SST correlation. This was done by selecting the +SST group as the 20 months which show the highest SST time coefficients but do not belong to the group with top 20 PNA projections. The −SST group is similarly selected. The +SST group and the −SST group are inclosed in the right and left solid boxes in Fig. 6, respectively.

Figure 7 indicates that the prediction spread for the +SST group is not significantly different from that of the −SST group, and there is almost no improvement for the time limit of predictability. In fact, both +SST and −SST groups show prediction spread close to the −PNA group. In other words, even with the presence of strong positive SST anomalies in the tropical Pacific, atmospheric predictability may not improve if the
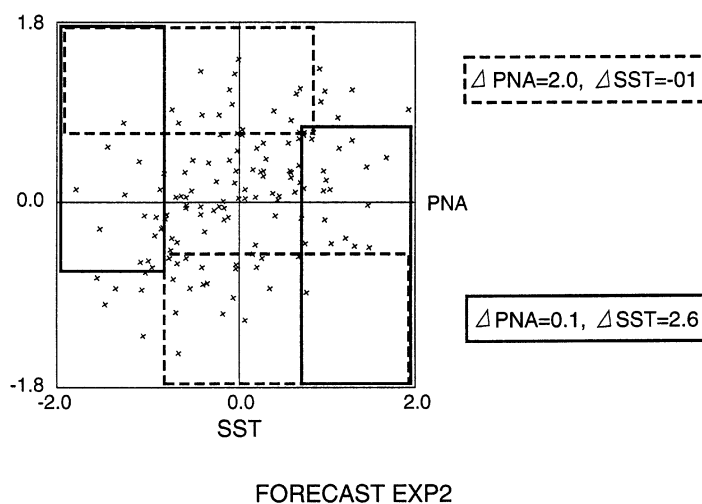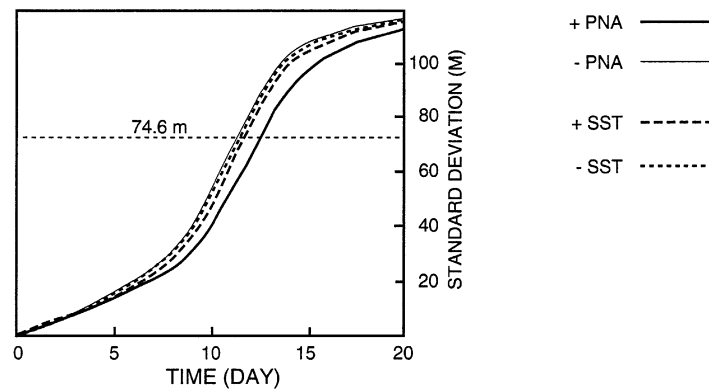

FORECAST EXP2

Fig. 6. Same as Fig. 4, except for EXP2. See text for more details.

FORECAST EXP2

Fig. 7. Same as Fig. 5, except for EXP2.

PNA pattern is in a weak phase. These results strongly suggest that the influence of the tropical SST anomalies on the predictability is only secondary and indirect through the SST and PNA correlation.

The difference in prediction spread S between the positive and negative phases of the PNA pattern is averaged over the 10-d period between the forecast day 5 and day 14 (mean ensemble standard deviation in $+$PNA phase less that in $-$PNA phase) for EXP1. Its geographic distribution is shown in Fig. 8. Most of the Northern Hemisphere is characterized by negative values. The largest negative contributions come from northwestern Atlantic and northeastern Pacific, offset by weaker positive values in the North American continent. The difference map for the SST groups is very similar to Fig. 8 (not shown).

To investigate further the regional characteristics of the atmospheric predictability, three areas are selected to represent the regions of northeastern Pacific, North American and northwestern Atlantic regions (Fig. 9). The prediction spread in EXP1 was spatially averaged for each of the three areas and then plotted against time. In northeastern Pacific (Area 1, Fig. 10a), the $+$PNA and $-$PNA groups show their typical behavior, with the $+$PNA group consistently outperforms the $-$PNA group over the entire period of the forecast. It is noted that the predictability continues to deteriorate even at day 20. For the North American continent (Area 2, Fig. 10b), the $-$PNA

group has better prediction spread than $+$PNA from day 2 to day 9 and again from day 14 to day 20, but a poorer spread from day 9 to day 14. The northwestern Atlantic region (Area 3, Fig. 10c) shows very similar features as Area 1, except a slight return of predictability! in the late prediction stage (after day 17), as indicated by the a decrease of the thick solid curve in Fig. 10c. These features highlight the variability of the prediction spread on the regional scale.

Considering the complexity of the GCM model and the number of factors that may influence the predictability of the ensemble forecast, it is difficult to conduct a comprehensive investigation of the physical mechanisms that cause the difference in error standard deviation between the positive and negative PNA phases. It is reasonable, however, to speculate that the activities of transient synoptic-scale eddies play an important role. Sheng et al. (1998) studied the dynamic forcing of the PNA pattern by the synoptic-scale eddies and found that the vorticity flux divergence anomaly is positively correlated with the PNA height field, especially in the upper troposphere. Transient eddies tend to strengthen the height anomalies associated with the PNA pattern both in the positive and negative phases. The high-frequency transients are almost impossible to predict over long term and their nonlinear interactions are the very ca! use of limited predictability of the atmosphere (Lorenz, 1963; 1969). In a straightforward attempt to explain the predictability difference, we will dem-
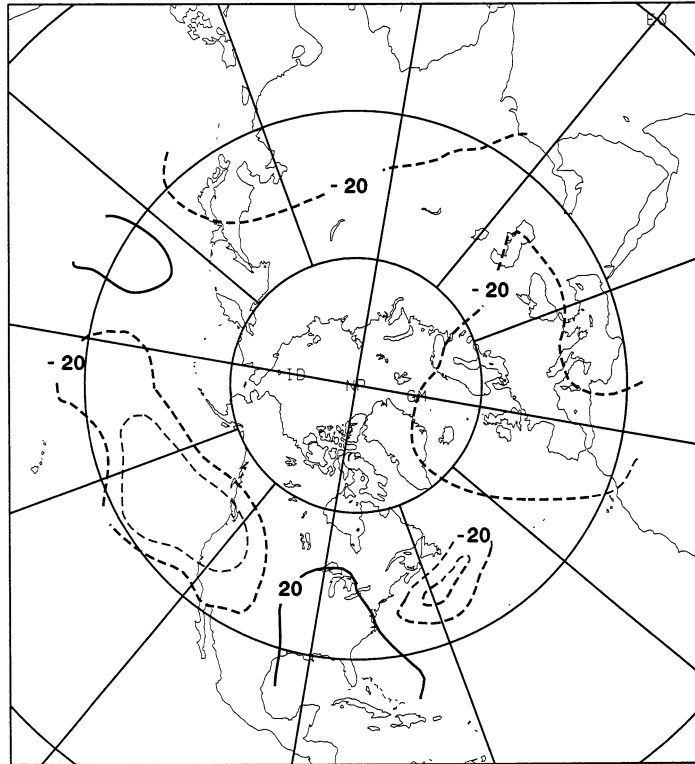
DIFFERENCE IN STANDARD DEVIATION (M)

Fig. 8. EXP1. Spatial distribution of the difference in standard deviation for the +PNA and −PNA groups.

onstrate that the influence of eddy forcing on the model height anomalies is stronger in the −PNA group than in the +PNA group.

To calculate the forcing by the vorticity flux we use a set of global, linearized, steady-state, quasi-nondivergent equations as a diagnostic model (refer to Sheng et al., 1998 for details):

Vorticity equation

$$J(\bar{\psi}, \nabla^2\psi) + J(\psi, \nabla^2\bar{\psi} + f) + \nabla \cdot (F \nabla\chi)$$
$$+ k_1\nabla^6\psi k_2\nabla^2\psi - F_\zeta = 0,$$

thermodynamic equation

$$J(\bar{\psi}, \Delta\Phi) + J(\psi, \Delta\bar{\Phi}) + \sigma\omega\Delta p + k_1\Delta\Phi$$
$$+ k_3\Delta\Phi = 0,$$

continuity equation

$$\nabla^2\chi\Delta p + \Delta\omega = 0,$$

balance equation

$$\nabla^2\Phi - \nabla \cdot (f\nabla\chi) = 0,$$

where the over-bar refers to the monthly average mean flow from the GCM, ψ is the stream function, J, the Jacobian operator, χ, the velocity potential, Φ, the geopotential, σ, the static stability parameter, ω, the vertical velocity in isobaric coordinates, p, pressure, R, the gas constant, and Δ, vertical finite difference. The horizontal biharmonic diffusion coefficient is denoted by k_1, the coefficients of Rayleigh friction and Newtonian cooling, by k_2 and k_3, respectively, and F_ζ, the sole forcing term, represents the eddy vorticity flux convergence. The linearized vorticity, balance and continuity equations are applied to the 250, 550 and 850 hPa levels, while the linearized thermodynamic equation is written on the intermediate 400 and 700 hPa levels. The system is expanded spectrally with a triangular
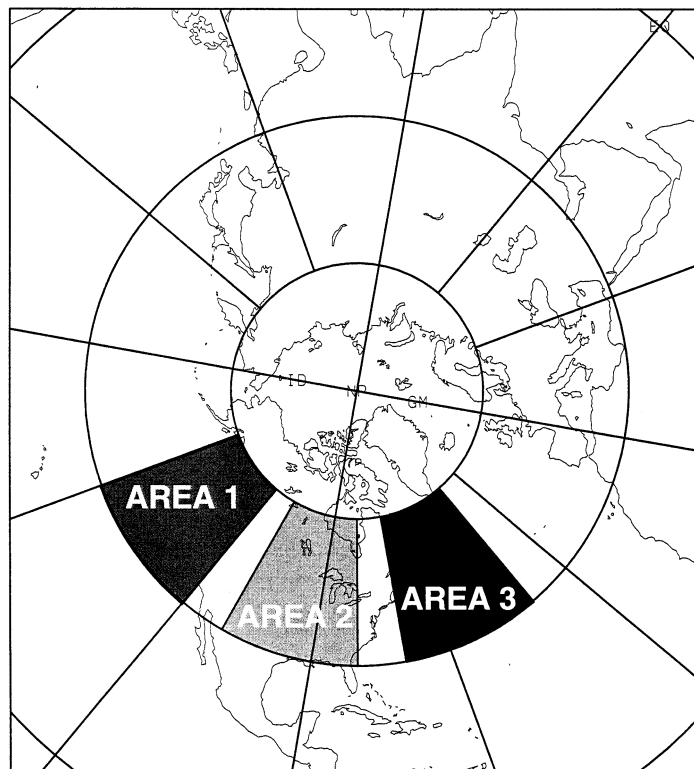
Fig. 9. Areas selected for illustration of regional features of atmospheric predictability.

truncation at two-dimensional wavenumber 20 (T20). The details of the model can be found in Sheng et al. (1998).

The forcing term F_ζ is calculated from the GCM output and averaged for the forecast period of 20 d. The response to the forcing as geopotential height anomalies, denoted as z'_r, is solved from the diagnostic model. This is done for every integration when the extended-range forecasts were made. According to Sheng et al. (1998), the response represents the forcing on the mean anomaly flow by the transient eddy vorticity flux. After z'_r is obtained, its covariance with the model height anomaly z' is computed. $\mathrm{Cov}(z', z'_r)$ is therefore a measure of the contribution of transient eddy forcing to the predicted height anomalies.

Figure 11 shows the difference in $\mathrm{Cov}(z', z'_r)$ between the $+$PNA group and $-$PNA group. For most of the Northern Hemisphere, the difference in $\mathrm{Cov}(z', z'_r)$ is negative, indicating that the overall contribution from the transient eddies is smaller in the positive PNA phase. It is also noted that the most negative values are found in the eastern Pacific and western Atlantic, with a positive region over the North American continent. This pattern is similar to the distribution of the difference in prediction spread between the $+$PNA and $-$PNA groups (Fig. 8). The sign and distribution of $\mathrm{Cov}(z', z'_r)$ indicate that, during the negative PNA phase, the transient eddies contribute more to maintaining height anomalies. These results, therefore, are consistent with our speculation that the atmospheric predictability is related to the transient eddy activities during the different phases of the PNA patterns. Lin and Derome (1996), using their three-level Q–G model, found that low-frequency anomalies extract less kinetic energy from the synoptic-scale eddies during the positive PNA phase. Their results are supported by our diagnostic model for the GCM prediction experiments.
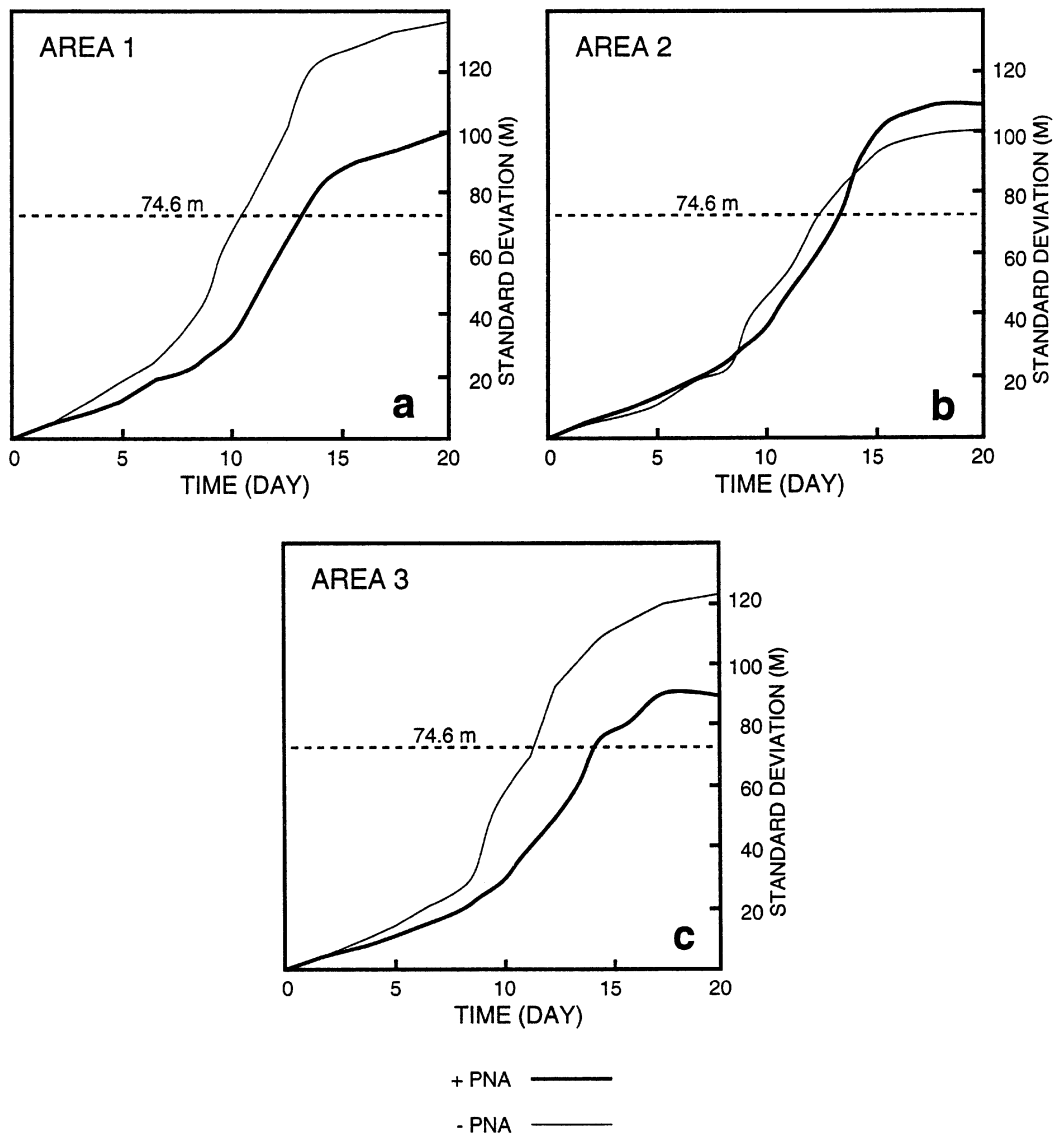
FORECAST EXP1

Fig. 10. EXP1. Prediction score as functions of time for selected areas.

5. Conclusions

Based on the 47-yr GISST integration of CCCma GCMII with specified boundary conditions, predictability experiments are conducted with selected initial conditions in an attempt to identify more predictable atmospheric states with the PNA pattern as the main indicator. The results can be summarized as follows:

(1) The CCCma GCMII reproduces, with reasonable fidelity in spatial structure, the PNA pattern in the GISST integrations. The model
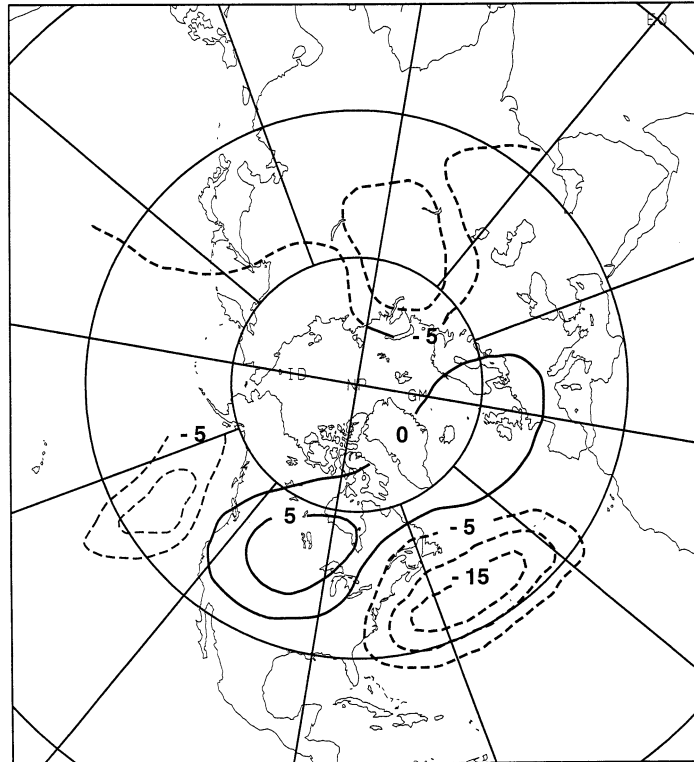
DIFFERENCE IN COVARIANCE (10 M*M)

Fig. 11. Distribution of the difference in between the +PNA and −PNA groups. contour interval 10 m².

PNA pattern has a good, although somewhat weak, correlation with the observed tropical SST anomalies.

(2) Extended-range forecasts initiated from strong positive PNA phases tend to have smaller prediction spread (higher predictability) than that initiated from strong negative PNA phases. The predictability limit differs by 1.4 d between the two groups. The GCM experiments on atmospheric predictability confirm the results from the three-level Q–G model obtained by Lin and Derome (1996).

(3) Extended forecasts initiated from months with strong positive tropical SST anomalies tend to have a smaller prediction spread (higher predictability) than that with negative tropical SST anomalies. Our results are consistent with the findings of Kumar et al. (2000) that changes in the spread of the atmospheric seasonal means are

more systematic for periods of warmer tropical SST anomalies.

(4) Cases with positive tropical SST anomalies but a weak PNA pattern, however, do not show a lower prediction spread than that with negative SST anomalies. The impact of SST anomalies on the atmospheric predictability is only secondary and indirect through tropical the SST's correlation with the PNA pattern.

(5) The difference in predictability is negative in the northwestern Atlantic and northeastern Pacific but positive over the North American continent.

(6) The steady-state solution of the three-level diagnostic model shows that the transient eddies have a stronger influence on the model anomalies during the negative PNA phase than that during the positive PNA phase.

In the present study, the CCCma GCMII with

sophisticated dynamic and physical processes is shown to have an improved atmospheric predictability in extended-range forecasts, if they are initiated from a strong positive phase of PNA pattern. It is noted that the predictability is measured in the context of a perfect model approach. Further studies are needed to investigate if this relationship holds for other GCMs and weather prediction models, as well as whether more accurate forecasts of observed atmospheric state can be made during the positive PNA phase. Other teleconnection patterns have also been searched for similar influence on predictability. With the exception of Western Pacific pattern, which has a good temporal correlation with the PNA pattern, we have had little success.

REFERENCES

Boer, G. J., McFarlane, N. A. and Lazare, M. 1992. Greenhouse gas-induced climate change simulated with the CCC second generation general circulation model. *J. Clim.* **5**, 1045–1077.

Boer, G. J., Flato, G. M. and Ramsden, D. 2000a. A transient climate change simulation with greenhouse gas and aerosol forcing: Projected climate change for the 21st century. *Clim. Dyn.* **16**, 427–450.

Boer, G. J., Flato, G. M., Reader, M. C. and Ramsden, D. 2000b. A transient climate change simulation with greenhouse gas and aerosol forcing: experimental design and comparison with the instrumental record for the twentieth century. *Clim. Dyn.* **16**, 405–425.

Branstator, G., Mai, A. and Baumhefner, D. 1993. Identification of highly predictable flow elements for spatial filtering of medium- and extended-range numerical forecasts. *Mon. Wea. Rev.* **121**, 1786–1802.

Bretherton, C. S., Smith, C. and Wallace, J. M. 1992. An intercomparison of methods for finding coupled patterns in climate data. *J. Climate* **5**, 541–560.

Charney, J. G., Fleagle, R. G., Lally, V. E., Riehl, H. and Wark, D. Q. 1966. The feasibility of a global observation and analysis experiments. *Bull. Am. Meteorol.* **47**, 200–220.

Chen, W. Y. 1990. Interannual variability of the NMC medium-range forecasts over the Pacific/ North America sector. *Mon. Wea. Rev.* **118**, 179–188.

Derome, J., Brunet, G., Plante, A., Gagnon, N., Boer, G. J., Zwiers, F. W., Lambert, S. J., Sheng, J. and Ritchie, H. 2001. Seasonal predictions based on two dynamical models. Atmosphere–Ocean, **39**, 485–501.

Epstein, E. S. 1969. Stochastic dynamic prediction. *Tellus* **21**, 739–759.

Flato, G. M., Boer, G. J., Lee, W. G., McFarlane, N. A., Ramsden, D., Reader, M. C. and Weaver, A. J. 2000. The Canadian Centre for Climate Modelling and Analysis global coupled model and its climate. *Clim. Dyn.* **16**, 451–467.

Horel, J. D. and Wallace, J. M. 1981. Planetary-scale atmospheric phenomena associated with the Southern Oscillation. *Mon. Wea. Rev.* **109**, 2080–2092.

Kumar, A., Barnston, A. G., Peng, P., Hoerling, M. P. and Goddard, L. 2000. Changes in the spread of the variability of the seasonal mean atmospheric states associated with ENSO. *J. Clim.* **13**, 3139–3151.

Lin, H. and Derome, J. 1996. Changes in predictability associated with the PNA pattern. *Tellus* **48A**, 553–571.

Leith, C. E. 1974. Theoretical skill of Monte Carlo forecasts. *Mon. Wea. Rev.* **102**, 409–418.

Lorenz, E. N. 1963. Deterministic nonperiodic flow. *J. Atmos. Sci.* **20**, 130–141.

Lorenz, E. N. 1969. The predictability of a flow which possesses many scales of motion. *Tellus* **21**, 289–307.

McFarlane, N. A., Boer G. J., Blanchet J-P. and Lazare M. 1992. The Canadian Climate Centre second-generation general circulation model and its equilibrium climate. *J. Clim.* **5**, 1013–1044.

Miyakoda, K., Sirutis, J. and Ploshay, J. 1986. One month forecast experiments – without anomaly boundary forcing. *Mon. Wea. Rev.* **114**, 2363–2401.

Palmer, T. N. 1988. Medium and extended range predictability and stability of the Pacific/North American mode. *Q. J.R. Meteorol. Soc.* **114**, 691–713.

Schubert, S. D. and Suarez, M. 1989. Dynamical predictability in a simple general circulation model: Average error growth. *J. Atmos. Sci.* **46**, 353–370.

Sheng, J., Derome, J. and Klasa, M. 1998: The role of transient disturbances in the dynamics of the Pacific North American Pattern. *J. Clim.* **11**, 523–536.

Sheng, J. and Zwiers, F. W. 1998. A time-interpolation scheme for bottom boundary conditions in atmospheric general circulation models. *Clim. Dyn.* **14**, 609–613.

Smagorinsky, J. 1969. Problems and promises of deterministic extended-range forecasting. *Bull. Am. Meteorol.* **50**, 285–311.

Zwiers, F. W., Wang, X. L. and Sheng, J. 1999. Effects of specifying bottom boundary conditions in an ensemble of atmospheric GCM simulations. *J. Geophys. Res.* **105, No. d6**, 7395–7315.